

Marker-less Reconstruction of Dense 4-D Surface Motion Fields using Active Laser Triangulation for Respiratory Motion Management

Sebastian Bauer, Benjamin Berkels, Svenja Ettl, Oliver Arold, Joachim Hornegger, Martin Rumpf

Abstract. To manage respiratory motion in image-guided interventions a novel sparse to dense registration approach is presented. We apply an emerging laser-based active triangulation (AT) sensor that delivers sparse but highly accurate 3-D measurements in real-time. These sparse position measurements are registered with a dense reference surface extracted from planning data. Thereby a dense displacement field is reconstructed which describes the 4-D deformation of the complete patient body surface and recovers a multi-dimensional respiratory signal for application in respiratory motion management. The method is validated both on real data from an AT prototype and synthetic data sampled from dense surface scans acquired with a structured light scanner and achieved a mean reconstruction accuracy of ± 0.22 mm when compared to ground truth data.

1 Introduction

In the context of small margin and high dose treatment, the management of intra-fractional respiratory motion is paramount for patients with thoracic, abdominal and pelvic tumors. Respiration-synchronized image-guided radiation therapy (IGRT) delivery techniques aim at tracking the tumor location and reposition the beam dynamically [1, 2]. To reduce additional radiation exposure, recent hybrid tumor-tracking techniques combine episodic radiographic imaging with continuous monitoring of external breathing surrogates based on the premise that the internal tumor position can be accurately predicted from external motion. The underlying correlation model can be established from a series of simultaneously acquired external-internal position measurements [2] or 4-D CT planning data [3]. Clinically available solutions for hybrid tumor-tracking [2, 4, 5] measure external motion using a single or a few passive markers on the patient’s chest as a low-dimensional surrogate. Thus, these techniques are incapable of depicting the full complexity of respiratory motion, they involve extensive patient preparation, and require reproducible marker placement with a substantial impact on model accuracy. Modern IGRT solutions that allow to monitor the motion of the complete external patient surface help to reduce correlation model uncertainties. In particular, optical range imaging (RI) technologies can acquire a dense 3-D surface model of the patient’s chest [6–8]. Based on the estimation of a dense displacement field representing the deformation of the instantaneous

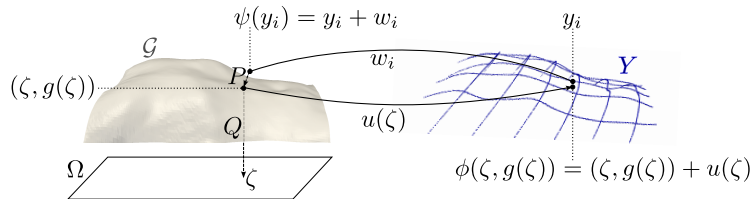


Fig. 1. Geometric configuration for reconstructing the dense deformation ϕ with $\phi(\zeta, g(\zeta)) = (\zeta, g(\zeta)) + u(\zeta)$ from sparse sampling data $Y = \{y_1, \dots, y_n\}$ and the approximate sparse inverse ψ with $\psi(y_i) = y_i + w_i$ (for a better visibility \mathcal{G} and Y have been pulled apart). Furthermore, the orthogonal projection P onto \mathcal{G} and the projection Q from the graph onto the parameter domain Ω are sketched.

torso surface w.r.t. a reference surface (either from RI or planning CT data), a highly accurate correlation model can be established [9, 10]. The deformation estimation from dense surface scans for application in RT has been investigated recently [11, 10]. Available RI-based IGRT solutions are capable of delivering dense surface information in a marker-less manner but focus on patient positioning, do not support dense sampling in real-time [6, 7] or at the cost of a limited field of view [8], often imply high costs in terms of hardware and are subject to measurement uncertainties due to the sampling principles e.g. active stereo [8] or swept lasers [6, 7]. The temporal resolution of these solutions may be insufficient to characterize respiratory motion [12].

In this paper, we propose a novel marker-less system based on a non-moving active laser triangulation (AT) sensor that delivers sparse but accurate measurements in real-time (30 Hz). Using prior patient shape knowledge from planning data, a variational model is proposed to recover a dense and accurate displacement field and to reconstruct a complete and reliable patient surface model at the instantaneous respiration phase. The variational model is discretized using a multi-linear Finite Element approach and the optimization is guided by a step-size controlled gradient flow to guarantee fast and smooth relaxation. The algorithm is evaluated on synthetic and real AT data from 16 subjects.

2 Method

In this section, we derive the variational model for the reconstruction of a dense displacement field from sparse measurements. Given is a reference shape $\mathcal{G} \subset \mathbb{R}^3$ extracted from planning data and the instantaneous body surface \mathcal{M} represented by a sparse sampling Y . For instance, let us assume that the AT sensor acquires a set of n measurements $Y = \{y_1, \dots, y_n\}$, $y_i \in \mathbb{R}^3$, arranged in a grid-like structure (Fig. 1). We assume that \mathcal{G} is given as a graph, i. e. there is a domain $\Omega \subset \mathbb{R}^2$ (usually associated with the plane of the patient table) and a function $g : \Omega \rightarrow \mathbb{R}$ such that $\mathcal{G} = \{(\zeta, g(\zeta)) \in \mathbb{R}^3 : \zeta \in \Omega\}$. Due to respiration, the intra-fractional sampling Y is not aligned with \mathcal{G} . Now, the goal is to estimate the unknown, non-rigid, dense deformation ϕ of \mathcal{G} with $Y \subset \phi(\mathcal{G})$. For this purpose, in a joint

manner, we estimate ϕ together with an inverse deformation ψ matching Y and \mathcal{G} in the sense that $\psi(Y) \subset \mathcal{G}$. Thereby, registering Y onto \mathcal{G} we solely deal with a sparse displacement field $(\psi(y_i))_{i=1,\dots,n}$ on the n positions measured by the AT. A geometric sketch of the registration configuration is depicted in Fig. 1. Estimating ψ allows us to establish a correspondence between the AT measurements and the reference patient surface, whereas the dense deformation ϕ enables the reconstruction of the complete instantaneous patient surface.

Let us fix some useful additional notation. We represent ψ by a vector of displacements $W = \{w_1, \dots, w_n\}$ with $\psi(y_i) = y_i + w_i$. Furthermore, the deformation ϕ is represented by a displacement $u : \Omega \rightarrow \mathbb{R}^3$ defined on the parameter domain Ω of the graph \mathcal{G} with $\phi(\zeta, g(\zeta)) = (\zeta, g(\zeta)) + u(\zeta)$. To quantify the matching of $\psi(Y)$ onto \mathcal{G} let us assume that the signed distance function d with respect to \mathcal{G} is precomputed in a sufficiently large neighborhood in \mathbb{R}^3 . We set $d(x) := \pm \text{dist}(x, \mathcal{G})$, where the sign is positive outside the body, i. e. above the graph, and negative inside. Then $\nabla d(x)$ is the outward pointing normal on \mathcal{G} and $|\nabla d(x)| = 1$. Based on this signed distance map d we can define the projection $P(x) := x - d(x)\nabla d(x)$ of a point $x \in \mathbb{R}^3$ in a neighborhood of \mathcal{G} onto the closest point on \mathcal{G} and compute the mismatch of $\psi(Y)$ and \mathcal{G} pointwise via $|P(\psi(y_i)) - \psi(y_i)| = |d(y_i + w_i)|$. Let us emphasize that we do not expect ψ to be equal to the projection P . Indeed, the computational results discussed below underline that it is the prior in the deformation ϕ which leads to general matching correspondences for a minimizer of our variational approach.

2.1 Definition of the Registration Energy

Now, we define a functional \mathcal{E} on dense displacement fields u and sparse vectors W of displacements such that a minimizer represents a suitable matching of the planning data and AT measurements:

$$\mathcal{E}[u, W] := \mathcal{E}_{\text{match}}[W] + \kappa \mathcal{E}_{\text{con}}[u, W] + \lambda \mathcal{E}_{\text{reg}}[u] \quad (1)$$

where κ and λ are nonnegative constants controlling the contributions of the individual terms. $\mathcal{E}_{\text{match}}$ denotes a term measuring closeness of $\psi(Y)$ to \mathcal{G} . The consistency functional \mathcal{E}_{con} is responsible for establishing the relation between both displacement fields. Finally, \mathcal{E}_{reg} ensures a regularization of the dense displacement u . The detailed definitions of these functionals are as follows.

Matching Energy. In order to measure closeness of $\psi(Y)$ to \mathcal{G} , we use the pointwise mismatch measure discussed above and define

$$\mathcal{E}_{\text{match}}[W] := \frac{1}{2n} \sum_{i=1}^n |d(y_i + w_i)|^2. \quad (2)$$

Consistency Energy. For a known instantaneous deformation ϕ of the patient surface \mathcal{G} and an exact deformation correspondence $\psi(Y) \subset \mathcal{G}$ of the AT measurement Y the identity $\phi(\psi(Y)) = Y$ holds. But for an arbitrary deformation ψ described by some vector of displacements W in general $\psi(Y) \not\subset \mathcal{G}$. To relate

ϕ and ψ in this case we have to incorporate the projection P because ϕ is only defined on \mathcal{G} . In fact, to ensure that $(\phi \circ P \circ \psi)(W) \approx W$ for a minimizer of the total energy we introduce the consistency energy

$$\mathcal{E}_{\text{con}}[u, W] := \frac{1}{2n} \sum_{i=1}^n |P(y_i + w_i) + u(Q P(y_i + w_i)) - y_i|^2, \quad (3)$$

where $Q \in \mathbb{R}^{3 \times 2}$ denotes the orthographic projection matrix with $Q(\zeta, g(\zeta)) = \zeta$. Here, we have used that $\phi(P(\psi(y_i))) = P(y_i + w_i) + u(Q P(y_i + w_i))$. Indeed, this definition of the consistency energy allows us to compute a dense smooth displacement of the patient planning surface even though only a sparse set of measurements is available.

Prior for the Displacement. To ensure smoothness of the deformation ϕ on \mathcal{G} we incorporate a thin plate spline type regularization of the corresponding displacement u [13] and define

$$\mathcal{E}_{\text{reg}}[u] := \frac{1}{2} \int_{\Omega} |\Delta u|^2 dx, \quad (4)$$

where $\Delta u = (\Delta u_1, \Delta u_2, \Delta u_3)$ and thus $|\Delta u|^2 = \sum_{k=1}^3 (\Delta u_k)^2$. Indeed, since our input data Y only implicitly provide information for ϕ on a sparse set, a first order regularizer is inadequate to ensure sufficient regularity for the deformation. Let us emphasize that (discrete) smoothness of the approximate inverse deformation ψ is implicitly controlled by the regularization of ϕ .

2.2 Numerical Optimization

To minimize the functional \mathcal{E} (Eq. 1), we apply a Finite Element approximation and optimize the functional using a gradient descent scheme. In particular, after an appropriate scaling of \mathcal{G} we choose $\Omega = [0, 1]^2$ and consider a piecewise bilinear, continuous Finite Element approximation on a uniform rectangular mesh covering Ω (we used a 129×129 grid). Furthermore, the signed distance function d is precomputed using a fast marching method [14] on a uniform rectangular 3-D grid covering the unit cube $[0, 1]^3$ and stored on the nodes of this grid. In the algorithm d and ∇d are evaluated using trilinear interpolation of nodal values. For the gradient descent, derivatives of the energy have to be computed numerically. The derivatives of $\mathcal{E}_{\text{match}}$ and \mathcal{E}_{con} w.r.t. w_j are given as:

$$\begin{aligned} \partial_{w_j} \mathcal{E}_{\text{match}}[W] &= \frac{1}{n} d(y_j + w_j) \nabla d(y_j + w_j) \\ \partial_{w_j} \mathcal{E}_{\text{con}}[u, W] &= \frac{1}{n} (P(y_j + w_j) + u(P_{\Omega}(y_j + w_j)) - y_j) \\ &\quad (DP(y_j + w_j) + \nabla u(Q P(y_j + w_j)) Q DP(y_j + w_j)) \end{aligned}$$

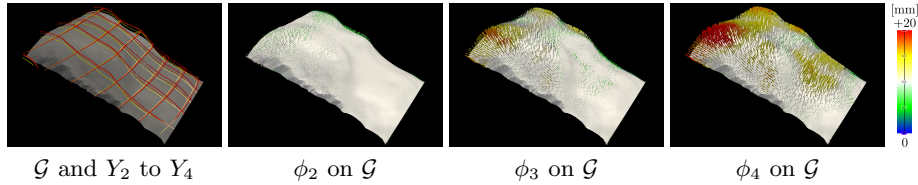


Fig. 2. Validation on real AT data. Estimation of ϕ_p transforming \mathcal{G} into \mathcal{M}_p , from AT sampling data Y_p . For the glyph visualization of ϕ_p on \mathcal{G} , $|u(\zeta)|$ is color coded [mm].

where DP denotes the Jacobian of the projection P . The variations of \mathcal{E}_{con} , \mathcal{E}_{reg} with respect to u in a direction $\vartheta : \Omega \rightarrow \mathbb{R}^3$ are given by

$$\begin{aligned} \langle \partial_u \mathcal{E}_{\text{con}}[u, W], \vartheta \rangle &= \frac{1}{n} \sum_{i=1}^n (P(y_i + w_i) + u(QP(y_i + w_i)) - y_i) \vartheta(QP(y_i + w_i)) \\ \langle \partial_u \mathcal{E}_{\text{reg}}[u], \vartheta \rangle &= \sum_{k=1}^3 \int_{\Omega} \Delta u_k \Delta_k \vartheta \, dx \end{aligned}$$

The evaluation of DP involves the Hessian $D^2d(x)$ of the distance function. One can either compute $D^2d(x)$ based on second order finite differences or - as actually implemented here - replace the projection direction in P by the already computed direction from the last update. Furthermore, the Laplacian of a Finite Element function is evaluated by the discrete Finite Element Laplacian. In the gradient descent scheme we stop iterating as soon as the energy decay is smaller than a threshold value ϵ ($\epsilon = 10^{-4}$ proved to be sufficient to achieve the accuracy reported below). For the first frame of the respiratory motion we initialize $u = 0$ and $w_j = P(y_j) - y_j$ leading to approx. 60 gradient descent steps on average. For all subsequent frames we take u computed in the previous step and $w_j = P(y_j) - y_j$ as initial data resulting in approx. 45 descent steps on average.

3 Experiments and Results

Experimental Setup. For validation of the method, we have used an eye-safe AT prototype that is based on a novel single-shot active triangulation principle [15]. The prototype acquires a sparse grid of 11×10 accurate 3-D sampling lines in real-time (30 Hz), using two perpendicular laser line pattern projection systems and a 1024×768 px resolution CCD chip. Within the measurement volume, the mean AT measurement uncertainty is $\sigma = 0.39$ mm. The evaluation dataset is composed of 32 datasets from 16 subjects, each performing abdominal and thoracic breathing, respectively. Per subject, we synchronously acquired both real AT data and surface data using a moderately accurate but rather dense structured light (SL) system with a resolution of 320×240 px. Both sensors were mounted at a height of 1.2 m above the patient table, at a viewing angle of 30° .

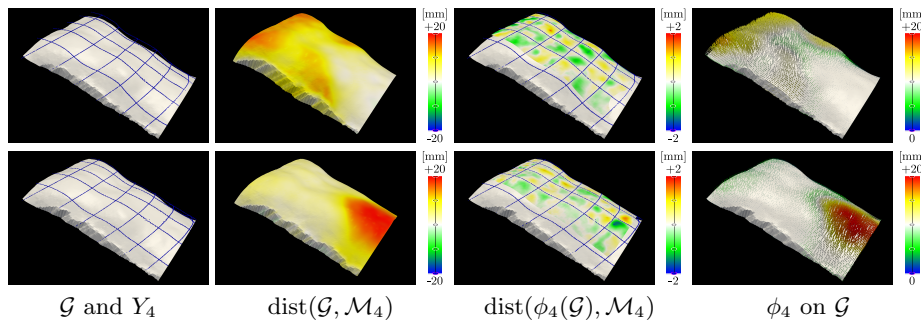


Fig. 3. Estimation of ϕ_p transforming \mathcal{G} into \mathcal{M}_p from realistic AT sampling data Y_p , for thoracic (top row) and abdominal respiration (bottom row). $p = 4$ represents the respiration state of fully inhale, roughly. For the glyph visualization of ϕ on \mathcal{G} , $|u(\zeta)|$ is color coded [mm]. Please note that the color coding differs by a factor of 10.

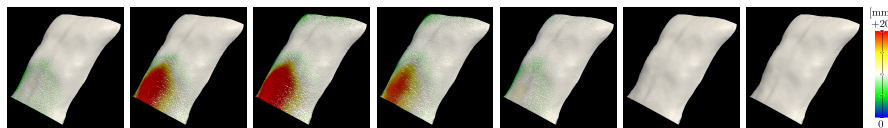


Fig. 4. Glyph visualization of ϕ_2 to ϕ_8 on \mathcal{G} for an abdominal respiration cycle.

AT and SL data were aligned using calibration. From each dataset, we extracted sparse AT measurements Y_p and dense SL meshes \mathcal{M}_p for 8 phases within one respiration cycle. In the experiments below, the subject’s body surface at full expiration \mathcal{M}_1 is considered as the given planning data \mathcal{G} . The model parameters were empirically set to $\kappa = 8 \cdot 10^{-1}$, $\lambda = 4 \cdot 10^{-8}$.

Validation on Real AT Data. Results for the reconstruction of ϕ_p for phase p on real AT data are given in Fig. 2. A quantitative evaluation on real AT and aligned SL data was unfeasible, as the SL camera exhibited local sampling artifacts (due to the underlying measurement principle and interferences between the laser grid (AT) and speckle pattern projections (SL) of the synchronously used modalities) which cause local deviations in the scale of several millimeters.

Quantitative Evaluation on Realistic AT Data. For quantitative evaluation, we developed a simulator for the generation of realistic AT sampling data from dense SL surfaces. For this purpose, the noise characteristics of our AT sensor prototype were measured in an optics lab and used to augment the synthetic sampling, providing realistic AT data. We considered the reconstruction of the displacement field ϕ_p from realistic AT data Y_p , $p = \{2, \dots, 8\}$ sampled from \mathcal{M}_p . An evaluation is given in Fig. 3 and the displacements for a full respiration cycle are shown in Fig. 4. The accuracy of the deformation estimation is assessed by the absolute error $|\text{dist}(\phi_p(\mathcal{G}), \mathcal{M}_p)|$ in Fig. 5 representing the mismatch between the transformed reference surface and ground truth surface. To discard boundary effects, the evaluation is performed within the central surface of interest covering the torso. Over all subjects and respiration phases, the

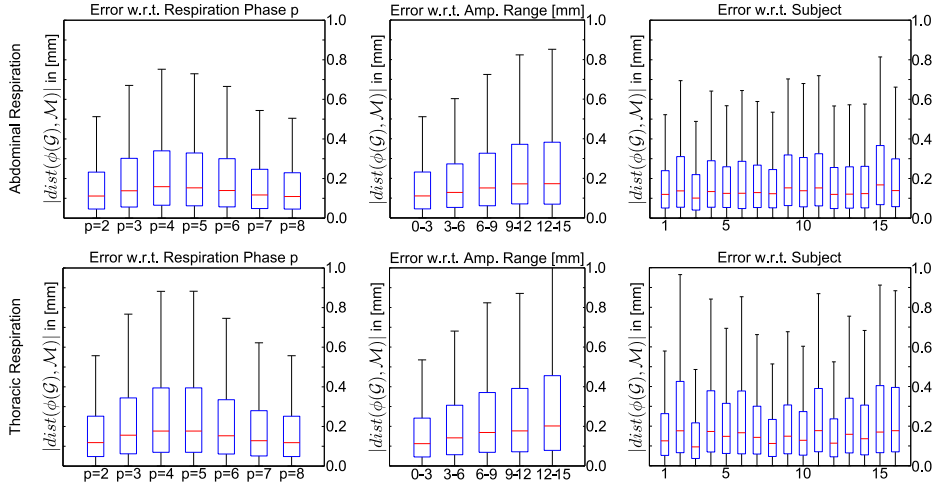


Fig. 5. Box plots of $|\text{dist}(\phi_p(\mathcal{G}), \mathcal{M}_p)|$ for realistic AT sampling data from 16 subjects, for abdominal (top row) and thoracic (bottom row) respiration. Given are plots (left) for different phases of the respiration cycle, (center) w.r.t. the respiration amplitude, and (right) for the individual subjects. Note that the reconstruction error scales approximately linearly with the respiration amplitude observing a peak at the respiration state of fully inhale (phase 4/5). The whiskers indicate that $>99\%$ of the residual error is <1 mm.

mean reconstruction error was 0.22 mm w.r.t. ground truth dense SL data. This indicates that the proposed method is capable of reliably recovering the dense and accurate displacement field from a sparse sampling of the instantaneous patient state using prior shape knowledge.

Runtime Performance. With our proof of concept implementation, a single gradient descent step on a single core of a Xeon X5550 2.67GHz CPU currently takes ≈ 60 ms. Over all subjects, we achieved total runtimes of 2.6 ± 0.7 s. As our proposed method exhibits an inherently high degree of data parallelism we further consider a GPU implementation.

4 Conclusions and Outlook

A key challenge in IGRT is respiratory motion. In this paper, a novel variational approach to marker-less reconstruction of dense non-rigid 4-D surface motion fields from sparse but accurate real-time AT sampling data has been introduced. In a study on 16 subjects, we demonstrated that the algorithm can precisely reconstruct the dense respiratory displacement field using prior shape knowledge from planning data, at a mean reconstruction accuracy of ± 0.22 mm. The implications of this work for RT motion management are manifold. The 4-D motion fields can be used as physically correct multi-dimensional respiration surrogates, as input for accurate external-internal motion correlation models, and to reconstruct the instantaneous body shape for patient positioning. Although we have

limited our discussion to RT, the approach holds great potential for motion-compensated tomographic reconstruction and image-guided interventions.

References

1. Depuydt, T., Verellen, D., Haas, O., Gevaert, T., Linthout, N., Duchateau, M., Tournel, K., Reynders, T., Leysen, K., Hoogeman, M., Storme, G., Ridder, M.D.: Geometric accuracy of a novel gimbals based radiation therapy tumor tracking system. *Radiotherapy and Oncology* **98**(3) (2011) 365–372
2. Hoogeman, M., Prvost, J.B., Nuyttens, J., Pll, J., Levendag, P., Heijmen, B.: Clinical accuracy of the respiratory tumor tracking system of the Cyberknife: assessment by analysis of log files. *Int J Radiat Oncol Biol Phys* **74**(1) (2009) 297–303
3. Verellen, D., Depuydt, T., Gevaert, T., Linthout, N., Tournel, K., Duchateau, M., Reynders, T., Storme, G., Ridder, M.D.: Gating and tracking, 4D in thoracic tumours. *Cancer/Radiotherapie* **14**(67) (2010) 446–454
4. Ford, E.C., Mageras, G.S., Yorke, E., Rosenzweig, K.E., Wagman, R., Ling, C.C.: Evaluation of respiratory movement during gated radiotherapy using film and electronic portal imaging. *Int J Radiat Oncol Biol Phys* **52**(2) (2002) 522–531
5. Willoughby, T.R., Forbes, A.R., Buchholz, D., Langen, K.M., Wagner, T.H., Zeidan, O.A., Kupelian, P.A., Meeks, S.L.: Evaluation of an infrared camera and X-ray system using implanted fiducials in patients with lung tumors for gated radiation therapy. *Int J Radiat Oncol Biol Phys* **66**(2) (2006) 568–575
6. Brahme, A., Nyman, P., Skatt, B.: 4D laser camera for accurate patient positioning, collision avoidance, image fusion and adaptive approaches during diagnostic and therapeutic procedures. *Medical Physics* **35**(5) (2008) 1670–1681
7. Moser, T., Fleischhacker, S., Schubert, K., Sroka-Perez, G., Karger, C.P.: Technical performance of a commercial laser surface scanning system for patient setup correction in radiotherapy. *Phys Med* **27**(4) (2011) 224–232
8. Peng, J.L., Kahler, D., Li, J.G., Samant, S., Yan, G., Amdur, R., Liu, C.: Characterization of a real-time surface image-guided stereotactic positioning system. *Medical Physics* **37**(10) (2010) 5421–5433
9. Fayad, H., Pan, T., Clement, J.F., Visvikis, D.: Correlation of respiratory motion between external patient surface and internal anatomical landmarks. *Med Phys* **38**(6) (2011) 3157–3164
10. Schaerer, J., Fassi, A., Riboldi, M., Cerveri, P., Baroni, G., Sarrut, D.: Multi-dimensional respiratory motion tracking from markerless optical surface imaging based on deformable mesh registration. *Phys Med Biol* **57**(2) (2012) 357–373
11. Bauer, S., Berkels, B., Hornegger, J., Rumpf, M.: Joint ToF image denoising and registration with a CT surface in radiation therapy. In: *Proceedings of SSVM*. Volume 6667 of LNCS., Springer (2011) 98–109
12. Waldron, T.: External surrogate measurement and internal target motion: Photogrammetry as a tool in IGRT. In: *ACMP Annual Meeting*. (2009) 10059
13. Modersitzki, J., Fischer, B.: Curvature based image registration. *Journal of Mathematical Imaging and Vision* **18**(1) (2003) 81–85
14. Russo, G., Smereka, P.: A remark on computing distance functions. *Journal of Computational Physics* **163** (2000) 51–67
15. Ettl, S., Arold, O., Yang, Z., Häusler, G.: Flying triangulation—an optical 3D sensor for the motion-robust acquisition of complex objects. *Appl. Opt.* **51**(2) (2012) 281–289